Relative contributions of sinking and non-sinking carbon to the downward carbon flux

Wei-Lei Wang[1], Frédéric A. C. Le Moigne[2,3], Robert Letscher[4], François W. Primeau[1], J. Keith Moore[1]

Corresponding author: Wei-Lei Wang, Department of Earth System Science, University of California at Irvine, Irvine, California, USA. (weilei.wang@gmail.com)

[1]Department of Earth System Science, University of California at Irvine, Irvine, CA 92697, USA.

[2]GEOMAR, Helmholtz Centre for Ocean Research Kiel, Kiel, Germany.

[3]Mediterranean Institute of Oceanography (MIO), UM110, CNRS, IRD, Aix-Marseille Université, Campus de Luminy, 13288, Marseille, France

[4]Earth Sciences and Ocean Process Analysis Laboratory, University of New Hampshire, Durham, NH 03824, USA

Abstract. The downward flux of organic carbon exported from the surface ocean is of great importance to the Earth's climate because it represents the major pathway for transporting CO_2 from the surface ocean and atmosphere into the deep ocean and sediments where it can be sequestered for a long time. Here we present global-scale estimates for the export fluxes of total, dissolved, and particulate organic carbon (TOC, DOC, and POC, respectively) constrained by observed thorium-234 (^{234}Th) activity and dissolved phosphorus (DIP) concentration in a global inverse biogeochemical model for the cycling of phosphorus and ^{234}Th. We find that POC export flux is low in the subtropical oceans, indicating that a projected expansion of the subtropical gyres due to global warming will weaken the gravitational biological carbon pump. We also find that DOC export flux is low in the tropical oceans, intermediate in the upwelling Antarctic zone and subtropical south Pacific, and high in the subtropical Atlantic, subtropical north Pacific, and productive subantarctic zone (SAZ). The horizontal distribution of DOC export ratio (F_{DOC}/F_{TOC}) increases from tropical to polar regions, possibly due to the detrainment of DOC rich surface water during mixing events into subsurface waters (increasing the strength of the mixed layer pump poleward due to stronger seasonality). Large contribution to the export flux from DOC implies that the efficiency with which photosynthetically fixed carbon is exported as particles may not be as large as currently assumed by widely used global export algorithms.

1. Introduction

The biological pump transfers a large amount of photosynthetically produced organic carbon from the surface ocean into subsurface waters that are isolated from the atmosphere [*Archer et al.*, 2000; *Eppley and Peterson*, 1979] a process that regulates atmospheric CO_2, and thus influences the Earth's climate [*Kwon et al.*, 2009]. Because particulate organic carbon (POC) has a fast sinking speed it is thought to be a key control on the strength of the biological carbon pump [e.g. *Alldredge et al.*, 1993; *Giering et al.*, 2014]. Consequently empirical relationships have been devised to relate temperature and satellite-based estimates of net primary production (NPP) to the ef-ratio, which is defined as the ratio of export production or new production to total primary production [*Dunne et al.*, 2005; *Henson et al.*, 2011; *Laws et al.*, 2011; *Guidi et al.*, 2015]. These empirical algorithms commonly assume that the ef-ratio is positively correlated to NPP and negatively correlated to sea surface temperature (SST). However, export fluxes estimated from different versions of these simple algorithms can vary by a factor of three (4 - 12 Pg C yr^{-1}), though part of the difference may be caused by the choice of export depth as well methodological and data coverage issues [*Henson et al.*, 2011]. Furthermore, these algorithms have been challenged by direct observations [e.g. *Lam and Bishop*, 2007; *Henson et al.*, 2012; *Maiti et al.*, 2013; *Cavan et al.*, 2015; *Laurenceau-Cornec et al.*, 2015; *Le Moigne et al.*, 2016] showing that in highly productive upwelling regions such as the Southern Ocean (high productivity low export ratio region) NPP is negatively correlated to the ef-ratio [*Maiti et al.*, 2013; *Laurenceau-Cornec et al.*, 2015]. Biome-specific fittings have therefore been developed to better predict export efficiency from NPP and SST [*Britten and Primeau*,

2016]. However, the biome-specific models based on different but plausible functional forms predict large differences (> 100%) that cannot be ruled out because of limited observation of POC export fluxes, especially in the Indian Ocean and Subtropical gyres [*Britten and Primeau*, 2016].

The importance of non-gravitational export pathways, such as those caused by physical subduction and/or zooplankton migration, are often ignored but *Boyd et al.* [2019] suggest that non-gravitational export pathways that acts on both sinking and suspended particles can account for as much carbon export as from the gravitational carbon pump. *Emerson* [2014] analyzed annual net community production (ANCP), which is equal to the export flux of organic matter over an annual cycle, at three time series sites (Hawaii Ocean Time-series (HOT), Bermuda Atlantic Time-series Study (BATS), and ocean Station Papa (OSP)). He concluded that POC export flux is 3-4 times lower than the mass balance estimates of ANCP, indicating the dominant roles played by non-sinking particle export, DOC export, and/or zooplankton migration. *Hansell et al.* [2009] estimated that DOC export contributes ∼20% of the biogenic carbon export from the surface ocean. *Letscher et al.* [2015] estimated a global DOC export flux of 2.28 Pg C yr^{-1} using the Biogeochemical Elemental Cycling (BEC) model with dissolved organic matter (DOM) cycling parameters optimized to best match a global compilation of DOM observations. *Roshan and DeVries* [2017] estimated a similar climatological DOC export flux by coupling a neural network extrapolated DOC field with an ocean circulation model. They suggested that the DOC export flux is highest in the subtropical gyres implying that the role of DOC in the biological pump will be enhanced in the future because the subtropical gyres are predicted to expand with global warming. A potential caveat pointed out by

Roshan and DeVries [2017] is that the DOC observations were mostly collected during the summer season in regions with relatively low NPP. The goodness of fit of their annual-averaged model to summer field data ($R^2 = 0.95$ overall) does not rule out the potential importance of seasonality, especially in the high-latitude oceans. In summary, DOC and non-sinking particle exports contribute a significant fraction of the total organic carbon export but the magnitude of this contribution remains uncertain as indicated by the inconsistency of the previous estimates. This motivates us to revisit the relative importance of the non-gravitational pathway.

Biogeochemical inverse models can in principle be used to estimate global scale carbon export. For example, *Teng et al.* [2014] used a coupled inverse model for phosphorus and carbon cycles constrained by DIC and DIP observations, and estimated regionally-varying C:P ratios, from which they estimated a global-scale total carbon export of 9.13 Pg C yr^{-1}. Using a similar approach, but for a model of the marine nitrogen and phosphorus cycles with a constant C:N ratio, *Wang et al.* [2019a] estimated a global carbon export of $\sim$12 Pg C yr^{-1}. However, both models are unable to accurately separate the contribution of sinking POC export from the total export. This is in part due to the fact that *Teng et al.* [2014] did not include organic matter constraint in their model. Whereas, *Wang et al.* [2019a] did use observed DON as a constraint but its weight in the objective function was small compared to those of DIP and DIN. More importantly, it is not clear from these studies if and how the C:P ratios might be different for DOC compared to POC. Here we use ^{234}Th observations to further constrain the relative contributions of DOC and POC to the total export.

^{234}Th has been widely used to estimate regional ocean POC export [*Black et al.*, 2018; *Buesseler et al.*, 1995]. Its successful application is due to its strong particle affinity and short decay half-life of 24.1 days, which make it an excellent tracer for surface ocean processes. In addition, its radioactive parent, ^{238}U, is a conservative tracer and almost uniformly distributed in the ocean, which offers ^{234}Th a constant source in the water column. *Henson et al.* [2011] made the first attempt to estimate global carbon export using ^{234}Th method. They constrained a thorium based export ratio ("ThE-ratio") using in-situ estimates of ^{234}Th-based export and satellite-derived SST and PP, and obtained a low POC export rate of 4 Pg C yr^{-1}. They then assumed that DOC export flux was 20% of total carbon export rate, and concluded that the globally integrated carbon export was 5 Pg C yr^{-1}, which on average is lower than previous inverse model and satellite-based estimates [e.g. *Laws et al.*, 2011; *Guidi et al.*, 2015; *Teng et al.*, 2014; *Wang et al.*, 2019a]. The inconsistency between ^{234}Th-based and satellite-based estimates provides a further motivation for our study.

Here we use a data-constrained ocean circulation model [*DeVries and Primeau*, 2011; *Primeau et al.*, 2013] coupled with a phosphorus (P) cycling model to extrapolate sparse ^{234}Th activity measurements (Table A1) to the global ocean and then use an estimate of the POC: ^{234}Th ratio to evaluate the global export of POC as well as its regional variations. The extrapolation of the ^{234}Th activity measurements is performed by optimizing a set of biogeochemical parameters (Methods, Fig. A1, and Table A2) to best match the database of ^{234}Th activity measurements. TOC export flux is diagnosed from the phosphorus model using previously estimated spatially-varying C:P ratios. We then obtain the DOC export flux from propagating the difference between the TOC and POC export fluxes in a Monte

Carlo run (See Methods and Fig. 1). This allows us to assess the relative importance of DOC export in high productivity low export regimes. We discuss the implications of DOC export flux for the efficiency of biological pump. Furthermore, because the model produces separate estimates for the contribution from the dissolved and particulate phases of both C and P, we are able to obtain separate global-scale estimates for the C:P ratio of non-sinking organic matter and sinking organic matter.

2. Methods

In a steady-state ocean with no sinking particles, ^{234}Th and its parent ^{238}U are expected to be in a secular equilibrium with the activity of ^{234}Th equal to that of ^{238}U. In the ocean, its insolubility and strong particle affinity enable thorium to easily become attached to sinking particles and be carried out of the surface ocean in a process known as particle scavenging. If the scavenging removal process is fast enough, it will cause a deficit in ^{234}Th activity relative to the ^{238}U activity. Since the abundance of particles decreases with depth, the scavenging strength also decreases with depth allowing ^{234}Th to reach secular equilibrium at depth.

By measuring ^{234}Th distribution at different depths and integrating its deficit relative to ^{238}U, and assuming a POC:^{234}Th ratio one can estimate POC flux [*Buesseler et al.*, 1992]. This approach has been applied under both steady and non-steady state [*Cochran et al.*, 2000; *Savoye et al.*, 2006; *Buesseler et al.*, 2009; *Cai et al.*, 2010].

2.1. Phosphorus model

We model phosphorous cycling by tracing its three phases, dissolved inorganic phosphorus [DIP], non-sinking organic phosphorus [DOP], and sinking particulate organic phos-

phorus [POP]. We use square brackets to denote concentration/activity. The governing equations for phosphorus cycle are as follow,

$$\begin{aligned}
\Big[\frac{d}{dt}+\mathbf{T}\Big][\mathrm{DIP}] &= -\boldsymbol{\gamma}[\mathrm{DIP}]+\kappa_{\mathrm{d}}[\mathrm{DOP}]+\kappa_{\mathrm{g}}([\mathrm{DIP}]-\overline{[\mathrm{DIP}]}_{\mathrm{obs}}),\\
\Big[\frac{d}{dt}+\mathbf{T}\Big][\mathrm{DOP}] &= \sigma\boldsymbol{\gamma}[\mathrm{DIP}]+\kappa_{\mathrm{p}}[\mathrm{POP}]-\kappa_{\mathrm{d}}[\mathrm{DOP}],\\
\Big[\frac{d}{dt}+\mathbf{S}\Big][\mathrm{POP}] &= (1-\sigma)\boldsymbol{\gamma}[\mathrm{DIP}]-\kappa_{\mathrm{p}}[\mathrm{POP}],
\end{aligned} \tag{1}$$

where κ_{d} is DOP respiration rate constants, and is optimized in the inversion. κ_{p} (30 day)$^{-1}$ is the particle dissolution rate constant. κ_g (10^6 yr)$^{-1}$ is a weak restoring rate coefficient used to set the mean phosphate concentration to $\overline{[\mathrm{DIP}]} = 2.17$ mmol/m^{-3}, the observed volume weighted mean DIP concentration. σ is a production partition parameter that determines how much new production is allocated to DOP and POP. γ is DIP uptake rate, which is modeled using satellite derived NPP and two adjustable parameters (α and β) as follows,

$$\gamma(\mathbf{r}) \equiv \begin{cases} \alpha \dfrac{\left[\frac{1}{r_{\mathrm{C:P}}}\frac{\mathrm{NPP}(\mathbf{r})}{\mathrm{NPP}_0}\right]^{\beta}}{\frac{[\mathrm{DIP}]_{\mathrm{obs}}(\mathbf{r})}{[\mathrm{DIP}]_0}}, & \text{if } z < z_c, \\ 0, & \text{otherwise,} \end{cases} \tag{2}$$

where $r_{\mathrm{C:P}}$ is carbon to phosphorus ratio, NPP_0 and $[\mathrm{DIP}]_0$ are set to 1 mmol C m^{-2} s^{-1} and 1 mmol m^{-3}, respectively, and are used to ensure α has dimensions of inverse time. z_c is euphotic zone depth, in the model, it is the depth of the first two layers ($\sim$73 m) [*Teng et al.*, 2014].

Non-sinking phosphate (DIP and DOP) are transported by advection and diffusion that are modeled using an advection-diffusion transport operator, $\mathbf{T}$, defined so that $\mathbf{T}[C] \equiv \nabla \cdot \Big(\vec{U}[C] - \mathbf{K}\nabla[C]\Big)$. This operator was optimized using multiple tracers, including

salinity, temperature, sea surface height, CFC11, pre-bomb radiocarbon, and phosphate [*DeVries and Primeau*, 2011; *Primeau et al.*, 2013]. The vertical transport of sinking particulate organic phosphorus is modeled using a particle flux divergence operator, $\mathbf{S}$, that is built based on the power law attenuation function known as Martin curve [*Fu and Primeau*, 2017]. The Martin curve exponential b values are optimized in inversion (Fig. A1).

2.2. Thorium model

We model thorium cycling by tracing its two phases, a "dissolved" phase ($[\mathrm{Th_d}]$) that is not associated with particles and a "particulate" phase ($\mathrm{Th_p}$) that is adsorbed on sinking particles. Dissolved ^{234}Th is produced by its conservative parent $\left([^{238}\mathrm{U}]\left(\frac{\mathrm{dpm}}{\mathrm{m}^{-3}}\right) = 78.6\mathrm{S} - 315, \text{where S is salinity}\right)$ via alpha decay [*Owens et al.*, 2011], and lost by its own alpha decay. It is also lost by adsorption onto particles, which is modeled as a product of [POP] and $[\mathrm{Th_d}]$ with an adjustable adsorption rate constant κ_1 (Eq. 3). Particulate thorium is returned back to the dissolved phase via particle dissolution and desorption, and also sinks in the water column.

The governing equations for thorium cycling are the following,

$$\begin{aligned}\left[\frac{d}{dt} + \mathbf{T}\right][\mathrm{Th_d}] &= \boldsymbol{\lambda}_{234}([^{238}\mathrm{U}] - [\mathrm{Th_d}]) + (\kappa_\mathrm{p} + \kappa_{-1})[\mathrm{Th_p}] - \kappa_1[\mathrm{POP}][\mathrm{Th_d}],\\ \left[\frac{d}{dt} + \mathbf{S}\right][\mathrm{Th_p}] &= -(\boldsymbol{\lambda}_{234} + \boldsymbol{\kappa}_\mathrm{p} + \boldsymbol{\kappa}_{-1})[\mathrm{Th_p}] + \kappa_1[\mathrm{POP}][\mathrm{Th_d}],\end{aligned} \tag{3}$$

where λ_{234} is the decay constant for ^{234}Th, $[^{238}\mathrm{U}]$ is uranium-238 activity in dpm m^{-3}, κ_1 and κ_{-1} are adsorption and desorption rate constants, respectively, which are optimized in the inversion.

Sinking of particulate ^{234}Th is modeled using the same flux divergence operator $\mathbf{S}$ as in the phosphorus model. Transport of dissolved ^{234}Th is modeled using advection and diffusion transport operator ($\mathbf{T}$).

2.3. Parameter optimization and error estimations

Parameter optimization is conducted using Bayesian inversion method [*Teng et al.*, 2014; *Wang et al.*, 2019a, b]. The observed DIP concentration and ^{234}Th activity are used to constrain the model. We obtain phosphorus (P) and thorium (Th) fields by solving the governing equations for P and Th (Eqs.1-3). The governing equations for P-cycle model are linear, and thus can be solved using direct matrix inversion. With POP concentration from the P model, the Th equations are also linear, and are therefore solved by direct matrix inversion. We minimize the difference between model outputs and observations by optimizing a set of parameters controlling P and Th cycle using the following objective function.

$$f = e_{\mathrm{P}}{}' \frac{1}{\mathbf{W_P}} e_{\mathrm{P}} + e_{\mathrm{Th}}^{'} \frac{1}{\mathbf{W_{Th}}} e_{\mathrm{Th}},$$

where $e_{\mathrm{Th}} = [\mathrm{Th}_{\mathrm{mod}}] - [\mathrm{Th}_{\mathrm{obs}}]$ and $e_{\mathrm{P}} = [\mathrm{DIP}_{\mathrm{mod}}] - [\mathrm{DIP}_{\mathrm{obs}}]$. $\mathbf{W_{Th}}$ and $\mathbf{W_P}$ are precision matrices for ^{234}Th and DIP. $\mathbf{W_{Th}}$ is defined using the following equation,

$$\mathbf{W_{Th}} = \frac{1}{\sigma_{\mathrm{Th}}^2} \mathbf{V},$$

where $\mathbf{V}$ is grid-box fractional volumes ($\mathbf{V} = \mathrm{diag}(\Delta V_i / \sum_i \Delta V_i)$), and σ_{Th} is defined,

$$\sigma_{\mathrm{Th}}^2 = ([\mathrm{Th}_{\mathrm{mod}}]) - \mu_{\mathrm{Th}})' \mathbf{V} (([\mathrm{Th}_{\mathrm{mod}}] - \mu_{\mathrm{Th}})$$

with

$$\mu_{\mathrm{Th}} = \frac{\Sigma([\mathrm{Th}_{\mathrm{obs}}] \mathbf{V_{Th}})}{\Sigma \mathbf{V_{Th}}},$$

where $\mathbf{V_{Th}}$ is grid box volume, and the subscript Th represents the grid boxes with ^{234}Th observations. The DIP weighing matrix $\mathbf{W_P}$ is defined similarly.

The optimization is conducted using Matlab's `fminunc` function, which is efficient because we are able to supply the first and second derivatives of the objective function. The optimization generally finishes within 100 iterations. The optimal model parameters are presented in Table A2 and Fig. A1. Parameter errorbars that correspond to ±1 standard deviation, are calculated according to the method described in *Wang et al.* [2019a]. We optimized a total of 17 model parameters to minimize the difference between model output and observations.

2.4. Calculation of carbon flux

The POC flux (F_{POC}) is calculated by integrating the deficit between [^{238}U] and [^{234}Th] over the studied depth and multiplying by a POC to ^{234}Th ratio (Eq. 4). Here we use a globally constant integration depth (z_0=114 m, depth of the upper three model layers), which is close to the suggested integration depth [*Buesseler et al.*, 2006].

$$F_{POC} = R_{\mathrm{POC:^{234}Th}} \times \lambda \int_0^{z_0} ([^{238}\mathrm{U}] - [^{234}\mathrm{Th}])dz. \quad (4)$$

The ratio of POC to ^{234}Th is calculated using the following empirical equation ($R_{\mathrm{POC:^{234}Th}} = 135.3 \times z^{-0.795}$) [*Owens et al.*, 2015]. Previous studies indicate that this ratio may have large seasonal, geographical, and depth variations, and can also vary significantly based on sampling methods [*Buesseler*, 1998]. However, by compiling data covering large geographical regions and different seasons, *Owens et al.* [2015] suggested that the variability of $R_{\mathrm{POC:^{234}Th}}$ decreases dramatically as depth increases, and becomes almost constant at depth of ∼100 m. In the present study, we apply the empirical relation-

ship at our studied depth of 114 m, and consider its possible variations in the uncertainty analysis (See next section). Thus, we are hypothesizing that a constant $R_{\mathrm{POC:}^{234}\mathrm{Th}}$ ratio produces an accurate carbon export estimate.

The POC flux below the first three layers is calculated based on the following power law function $\left(F_{POC}(z) = F_{POC}(z_0)\,(z/z_0)^{-b}\right)$ [*Martin et al.*, 1987], where z_0 is the reference depth (114 m), z is the depth where POC flux is calculated, and b is Martin curve exponentials that are optimized in the model (Fig. A1).

Total carbon export is diagnosed from the phosphorus model (See Fig. 1), which is constrained using both phosphate concentration and ^{234}Th activity. We first calculate total organic phosphorus (TOP) export based on an adjoint method [*Primeau et al.*, 2013], which tracks the export and subsequent remineralization of DOP and POP. Only DOP and POP respired/dissolved below the studied depth is counted as export. We then convert total phosphorous (DOP+POP) export to total carbon export by imposing spatially variable C:P ratios. To make this ratio more robust, we averaged the estimated C:P ratios from *Teng et al.* [2014] and *Wang et al.* [2019a] (Table 1).

2.5. Uncertainty analysis

The uncertainty analysis is conducted using a Monte Carlo method. Errors from three major sources are considered: 1) Model parameters and their associated error bars, 2) C:P ratio that is used to convert total phosphorus export to carbon export, and 3) POC to ^{234}Th ratio. Parameters are drawn randomly from a normal distribution with mean defined by optimal model parameters and variance defined by the covariance matrix. The C:P ratio from *Teng et al.* [2014] is selected randomly using the regional errorbars quoted in their paper. The POC to ^{234}Th ratio is drawn from a normal distribution with a mean

defined by POC:Th = $135.3z^{-0.795}$ at $z = 114$ m and a variance of 0.25, which creates a range between ∼2.3 to ∼4.0 that is consistent to Fig. 8 of Ref.[*Owens et al.*, 2015]. In the Monte Carlo analysis, we recalculate TOC and POC export fluxes based on parameters from each random drawn. DOC export flux is calculated as the difference between TOC and POC export fluxes at each iteration. We report median values and 95% confidence intervals that are based on a sample size of 1000.

3. Results and discussion

3.1. Global distribution of ^{234}Th

Overall, our model shows a reasonably good agreement with available ^{234}Th activity measurements (R^2= 0.46, Fig. A2b), the other 54% of variance can partially be explained by seasonal variability. Spatially, our model results correlate well with observations (Fig. 2), ^{234}Th activity (which is inversely proportional to the export flux of particles) is generally high in subtropical gyres, low to intermediate in the Southern Ocean and high in productive coastal regions. From the first (0-36 m) to third layer (73-114 m), ^{234}Th activity increases, indicating that scavenging strength becomes weaker, and ^{234}Th and ^{238}U are approaching secular equilibrium (See also Fig. A3).

3.2. Particulate Carbon export fluxes

Globally integrated, we estimate a POC export flux rate of 4.81 (95% CI 4.00-5.52) Pg C yr^{-1} (Fig. 3) at the bottom of the third grid box (114 m). If we scale up the export flux to 100 m using Martin curve function and the optimal b values (Fig. A1), our estimate becomes to 5.28 (95% CI 4.39-6.06) Pg C yr^{-1}. While our globally integrated POC export flux estimate disagrees with previous estimates taken individually, it is consistent with

the ensemble of previous estimates at the same reference depth (100 m). For example, *Harrison et al.* [2018] reported a high global POC export rate of 6.60-6.71 Pg C yr^{-1} whereas *Henson et al.* [2011] obtained a low rate of ∼4 Pg C yr^{-1} by scaling up ^{234}Th based measurements to the whole ocean using a relationship between satellite derived sea surface temperature and POC export observations. *Letscher et al.* [2015] calculated a POC export rate of 6.6 Pg C yr^{-1} by incorporating optimized DOM recycling parameters into a biogeochemistry model. More importantly, our POC export flux estimates are highly correlated with the in situ measurements [*Mouw et al.*, 2016], which consist mostly of sediment trap data of which only 4% are determined using the ^{234}Th method (Fig. 4). Geographically, POC flux is high in upwelling and subpolar regions and low in subtropical (Fig. 5a).

3.3. Total Carbon export fluxes

Our globally integrated TOC export is 7.74 (95% CI 7.53-7.97) Pg C yr^{-1} at the depth of 114 m, this number can be scaled up by ∼10% to 8.51 Pg C yr^{-1} at 100 m if we apply the same scaling factor that was used for the POC flux. However, this is a very coarse calculation, because the respiration from DOC is not expected to follow the same Martin curve decay function as used for POC. This estimate of the TOC export flux rate is within the (very wide) range of previous model and satellite based estimates (5-14 Pg C yr^{-1}, Table 1 of *Emerson* [2014]). We compared our regional estimates to those of *Emerson* [2014], who estimated export in four separate biomes: tropical (0-15°), subtropical (15-30°), subtropical/subpolar (30-45°), and subpolar (45-60°). We find that our mean export fluxes for each biome are in agreement (Fig. 6).

There are no experimentally determined large-scale annual TOC export flux estimates, because extensive sampling is needed to resolve the seasonal cycle. Thus reliable ANCP estimates are only available at time-series stations. We thus compared our TOC export flux rate with those measured at HOT, BATS, and OSP using mass balance calculations. Our model results (median with 95% CI) have overlapping errorbars with mass balance estimates at HOT ($61.5^{68.8}_{57.9}$ (this study) vs 82.2±23.0 mg C m^{-2} day^{-1}), at OSP ($57.9^{65.1}_{54.3}$ (this study) vs 75.6±19.7 mol C m^{-2} day^{-1}), and at BATS station ($86.8^{94.1}_{75.9}$ (this study) vs 124.9±39.5 mg C m^{-2} day^{-1}) [*Emerson*, 2014], when we scale our TOC export flux to 100 m (see above discussion). Our results show that it is critical to report the assumed reference depth explicitly along with the export flux. Based on our optimal b values, a ∼14 m depth difference (114 m compared to 100 m) can result in a ∼10% difference in export flux [*Henson et al.*, 2011]. The export flux difference caused by depth differences can be even larger if we extrapolate to shallower depths due to the negative exponent in the power law model for the flux attenuation.

3.4. Dissolved Carbon export fluxes

The DOC definition in our model is slightly different from conventional operationally defined DOC, which is based on filter pore size. In our model, DOC is non-sinking organic matter that can be transported by advection and diffusion. Our DOC export flux (Fig. 5c) is low in tropical regions, and high in subtropical Atlantic, subtropical north Pacific and high production Subarctic zone, and intermediate in the upwelling Antarctic zone and subtropical south Pacific. Smaller hotspots are also observed in the Peruvian, Mauritanian, Benguela, and Arabian Sea upwelling regions. Our globally integrated DOC export at 114 m is 2.9 (95% CI: 2.4-3.5) Pg C yr^{-1} (Fig. 3). *Hansell et al.* [2009]

estimated a DOC flux of 1.9 Pg C yr^{-1} out of 100 m by considering vertical velocities, mixing coefficients, and DOC concentrations. *Roshan and DeVries* [2017] estimated a global DOC flux from 74 m of 2.31 $\pm$0.60 Pg C yr^{-1}. *Letscher et al.* [2015] reported their estimate of 2.28 Pg C yr^{-1} (25% of the model TOC export flux) from 100 m. Because our DOC includes small non-sinking particles, our estimate is on the high end of previous estimates. It also represents the largest proportion to the total export of organic carbon ever obtained (38% vs 25% respectively).

We calculated zonally averaged DOC export proportion (DOC export flux over TOC export flux) for the four biomes (see above section for details) as in *Emerson* [2014]. We find that the mean DOC export ratio increases from 24% at equatorial regions, to 39% at subtropical regions, and to 50% and 44% at subtropical/subpolar and subpolar regions, respectively. Our poleward increasing DOC export ratios are consistent with the mixed layer pump mechanism [*Dall'Olmo et al.*, 2016; *Gardner et al.*, 1995]. The mixed layer pump invokes diurnal and/or seasonal variation of the mixed layer depth as a mechanism for exporting DOC or small non-sinking particles [*Dall'Olmo et al.*, 2016; *Gardner et al.*, 1995]. Deepening of the mixed layer brings DOC below the euphotic zone, subsequent mixed layer shoaling due to restratification by warming isolates DOC at depth. High latitude oceans experiencing the large seasonality are expected to have the strongest mixed layer pump [*Dall'Olmo et al.*, 2016].

Our DOC export flux pattern is quite similar to the net DOC removal rate (equivalent to DOC export flux) estimated based on the U.S. Climate Variability and Predictability (CLIVAR) DOC observations *Hansell et al.* [2012]. For example, both show DOC export flux is the highest in the subtropical north Atlantic, high in subantarctic ocean,

low/intermediate in the Antarctic zone, low in tropical oceans. Our results are also consistent with *Roshan and DeVries* [2017] in the tropical oceans, the Atlantic Ocean, and the subtropical north Pacific. However, our estimated fluxes show a strikingly different pattern in the Southern Ocean and in upwelling regions (Fig. 5c and Fig. 2b of *Roshan and DeVries* [2017]). *Roshan and DeVries* [2017] extrapolate DOC concentrations mostly sampled during the summer season to the global ocean by applying an artificial neural network (ANN) reconstruction method, which is trained using annually-averaged climatological means of temperature, salinity, oxygen, and nutrient data. They then diagnose the DOC production rate and export flux by coupling the reconstructed DOC concentration field to a global ocean circulation model. One major limitation of their method is that the DOC concentration data used to train the neural network is mostly from summertime field measurements which biases the estimated export in regions with a strong seasonal cycle. While ^{234}Th measurements used in this study were taken from different seasons (Table A1). We hypothesize that both the similarities and differences between our model and that of *Roshan and DeVries* [2017] can be explained by the sampling bias. First, the agreement in the tropical oceans is due to the weak seasonality in low latitudes, reducing the bias induced by applying summer time values for the annual average. Second, the similarity in the North Atlantic Ocean is due to the fact that in that basin, unlike the rest of the ocean, the sampling frequency is high enough to resolve the seasonal cycle. Third, the difference in the Southern Ocean can again be attributed to the presence of a strong and poorly resolved seasonal cycle, although poor spatial resolution might also be a contributor (Fig. 1 of *Roshan and DeVries* [2017]).

3.5. C:P ratios

With the optimal b values and an assumed particle dissolution rate constant, one can estimate particle sinking velocity[*Kriest and Oschlies*, 2008], with which POP sinking flux can be calculated given the POP distribution from the P cycle model (Fig. 1). We have POC flux diagnosed from ^{234}Th flux and $R_{\mathrm{POC:}^{234}\mathrm{Th}}$ ratio. We then compute C:P ratio of sinking particles for each region reported in *Teng et al.* [2014]. C:P ratio of dissolved organic matter is the ratio between DOC and DOP fluxes (Table 1).

Geographically, C:P ratio for both particulate and dissolved organic matter is high in subtropical gyres, and low in the Southern Ocean and equatorial upwelling regions. The North Atlantic gyre displays the highest C:P ratio in both dissolved and particulate fluxes. Another noticeable feature is that the the C:P ratio in the flux of dissolved organic matter is higher than in the flux from particles. This is in agreement with the finding of *Letscher et al.* [2015]. In addition, our C:P ratio is highly consistent to the ones estimated in *Letscher and Moore* [2015] with strongly overlapping errorbars (Table 1).

3.6. Ecological implications

Our results shed light on the conundrum of the low POC export in high production regions. The export efficiency calculated based on in-situ measurements of primary production and POC export flux [*Maiti et al.*, 2013] contradicts the empirical relationships that relate the ef-ratio to temperature and total primary production [*Laws et al.*, 2011, 2000]. Ecologically, four hypotheses are proposed to explain the occurrence of low particle export in high PP regions [*Le Moigne et al.*, 2016; *Laws and Maiti*, 2019]:

- H1 Primary production (PP) is exported not only as particles but also as DOC,

- H2 Strong surface microbial recycling even in low temperature regions,
- H3 Grazing-mediated export that varies inversely with PP (low grazing in high PP, so virtually no zooplankton mediated export).
- H4 A time lag between primary production and export at the base of euphotic zone.

For a given PP, these processes (acting individually or together) all decrease the amount of POC exported gravitationally. This could explain why high ef-ratios are very rarely observed in highly productive regions.

At the Station ALOHA, the negative relationship disappears when primary produciton and export were averaged over a long time frame (H4) [*Laws and Maiti*, 2019]. In the Southern Ocean, the observed low export efficiency may be explained by H2 and H3 [*Le Moigne et al.*, 2016]. However, our high/intermediate DOC export flux in the Southern Ocean indicates that H1 may also be an explanation for the low POC export efficiency observed here. The different conclusions between our model and *Le Moigne et al.* [2016] could be explained by the fact that *Le Moigne et al.* [2016] only examined the diffusive flux of DOC in summer when the water column is stratified while our model provides an annual average. We therefore hypothesize that in addition to surface microbial recycling and grazing-mediated export, which may dominate in summer only, on the annual scale, the export of DOC may be an important process during observed high productivity low export regimes. Elsewhere, in the eastern equatorial Pacific, there are also DOC export hotspots (Fig. 5c). This may indicate that H2 (microbial remineralization of carbon in the surface ocean) prevails in these high productivity warm waters. H3 has yet to be tested in warm high PP regions; however, global distribution of macrozooplankton abundance/biomass indicates that zooplankton stocks are not necessarily different in those regions relative to

the adjacent low PP warm waters [*Moriarty et al.*, 2013]. This indicates that H3 may not prevail in warm high PP regions. Our results suggest that that the causes of low POC export in high productivity regimes are not unique, and that they may vary regionally and seasonally. Most global carbon export models and algorithms do not account for the export of DOC [*Guidi et al.*, 2015; *Laws et al.*, 2000; *Siegel et al.*, 2014]. The contribution from DOC is typically included by simply adding an assumed portion to POC export flux [e.g. *Henson et al.*, 2011]. However, *Emerson* [2014] found that POC export is only a small fraction of ANCP at three time series stations. A better understanding of the various pathways associated to the gravitational biological carbon pump should help decipher what controls the efficiency and the magnitude of carbon export [*Cavan et al.*, 2015; *Laurenceau-Cornec et al.*, 2015; *Le Moigne et al.*, 2016]. Given the importance of the annual DOC export flux in certain regions (Fig. 5c) relative to the gravitational flux, we suggest that DOC export flux should also be included in future effort to model the global strength of the biological carbon pump, and that algorithm potentially considering DOC export flux need more development.

Our results have multiple implications to the global marine carbon cycle. First, a large percentage of carbon is exported in the form of DOC in high latitude oceans. Future global warming is expected to further stratify the ocean and weaken ocean mixing, thus a decreased DOC export flux is expected for the high latitude oceans. If DOC export reduces, other mechanisms such as microbial remineralization in the surface ocean may become dominant factors. Surface DOC recycling will retain nutrients and carbon in the upper ocean, and thus decrease the potential role of the ocean as a global carbon sink. Second, a low POC export rate is found in the subtropical oceans. Future expansion

of these regions due to global warming will also decrease gravitational carbon export. However, this reduction may be compensated or even overcame by the higher C:P ratios in the gyres. Lastly, on an annual basis, a large fraction of primary production is exported via DOC with higher C:P ratios compared to POC, which offers a possible explanation for the observed low POC export (relative to the observed NPP) in high latitude oceans.

Acknowledgments. We sincerely thank all GEOTRACES scientists who made related data available. We appreciate the financial support provided by the Division of Ocean Sciences of the US National Science Foundation (OCE-1436922). W.-L. Wang, R.T.L., F.W.P. and J.K.M. also acknowledge support from the US Department of Energy Office of Biological and Environmental Research (DE-SC0016539). Le M. acknowledge support by a DFG Fellowship of the Excellence Cluster The Future Ocean (CP1403 to F.A.C.L.M.). The code for the inverse model and carbon export flux data are available at DOI: 10.5281/zenodo.2651656. The ^{234}Th data used to constrain the model is from the cited sources (Table A1) and GEOTRACES website: https://www.egeotraces.org. The DIP data is from World Ocean Atlas 2013 [*Zweng et al.*, 2013; *Garcia et al.*, 2014].

Competing Interests:

The authors declare that they have no competing financial interests.

References

Alldredge, A. L., U. Passow, and B. E. Logan (1993), The abundance and significance of a class of large, transparent organic particles in the ocean, *Deep Sea Research Part I: Oceanographic Research Papers*, *40*(6), 1131–1140.

Archer, D., A. Winguth, D. Lea, and N. Mahowald (2000), What caused the glacial/interglacial atmospheric pCO_2 cycles?, *Rev. Geophys.*, *38*(2), 159–189.

Black, E. E., K. O. Buesseler, S. M. Pike, and P. J. Lam (2018), ^{234}Th as a tracer of particulate export and remineralization in the southeastern tropical Pacific, *Mar. Chem.*, *201*, 35–50.

Boyd, P. W., H. Claustre, M. Levy, D. A. Siegel, and T. Weber (2019), Multi-faceted particle pumps drive carbon sequestration in the ocean, *Nature*, *568*(7752), 327.

Britten, G. L., and F. W. Primeau (2016), Biome-specific scaling of ocean productivity, temperature, and carbon export efficiency, *Geophys. Res. Lett.*, *43*(10), 5210–5216.

Buesseler, K. O. (1998), The decoupling of production and particulate export in the surface ocean, *Global Biogeochem. Cycles*, *12*(2), 297–310.

Buesseler, K. O., M. P. Bacon, J. K. Cochran, and H. D. Livingston (1992), Carbon and nitrogen export during the JGOFS North Atlantic bloom experiment estimated from ^{234}Th:^{238}U disequilibria, *Deep-Sea Res. I:*, *39*(7/8), 1115–1137.

Buesseler, K. O., J. A. Andrews, M. C. Hartman, R. Belastock, and F. Chai (1995), Regional estimates of the export flux of particulate organic carbon derived from thorium-234 during the JGOFS EqPac program, *Deep-Sea Res. II*, *42*(2-3), 777–804.

Buesseler, K. O., J. Andrews, S. M. Pike, M. A. Charette, L. E. Goldson, M. A. Brzezinski, and V. Lance (2005), Particle export during the Southern Ocean iron experiment

(SOFeX), *Limnol. Oceanogr.*, *50*(1), 311–327.

Buesseler, K. O., C. R. Benitez-Nelson, S. Moran, A. Burd, M. Charette, J. K. Cochran, L. Coppola, N. Fisher, S. Fowler, W. Gardner, et al. (2006), An assessment of particulate organic carbon to thorium-234 ratios in the ocean and their impact on the application of ^{234}Th as a POC flux proxy, *Mar. Chem.*, *100*(3-4), 213–233.

Buesseler, K. O., C. Lamborg, P. Cai, R. Escoube, R. Johnson, S. Pike, P. Masque, D. McGillicuddy, and E. Verdeny (2008), Particle fluxes associated with mesoscale eddies in the Sargasso Sea, *Deep-Sea Res. II*, *55*(10-13), 1426–1444.

Buesseler, K. O., S. Pike, K. Maiti, C. H. Lamborg, D. A. Siegel, and T. W. Trull (2009), Thorium-234 as a tracer of spatial, temporal and vertical variability in particle flux in the North Pacific, *Deep-Sea Res. I*, *56*(7), 1143–1167.

Cai, P., W. Chen, Z. M. Dai, D. Wan, Q. Wang, T. Li, Tang, and D. Lv (2008), A high-resolution study of particle export in the southern South China Sea based on ^{234}Th:^{238}U disequilibrium, *J. Geophys. Res.*, *113*(C04019).

Cai, P., M. Rutgers van der Loeff, I. Stimac, E. M. Nthig, K. Lepore, and S. B. Moran (2010), Low export flux of particulate organic carbon in the central Arctic Ocean as revealed by ^{234}Th ^{238}U disequilibrium, *J. Geophys. Res.*, *115*(C10).

Cavan, E., F. A. Le Moigne, A. Poulton, G. Tarling, P. Ward, C. Daniels, G. Fragoso, and R. Sanders (2015), Attenuation of particulate organic carbon flux in the scotia sea, southern ocean, is controlled by zooplankton fecal pellets, *Geophys. Res. Lett.*, *42*(3), 821–830.

Charette, M. A., S. B. Moran, and J. K. Bishop (1999), 234Th as a tracer of particulate organic carbon export in the subarctic northeast Pacific Ocean, *Deep-Sea Res. II*, *46*(11-

12), 2833–2861.

Cochran, J. K., K. O. Buesseler, M. P. Bacon, H. W. Wang, D. J. Hirschberg, L. Ball, J. Andrews, G. Crossin, and A. Fleer (2000), Short-lived thorium isotopes (^{234}Th, ^{238}Th) as indicators of POC export and particle cycling in the Ross Sea, Southern Ocean, *Deep-Sea Res. II*, *47*, 3451–3490.

Coppola, L., M. Roy-Barman, S. Mulsow, P. Povinec, and C. Jeandel (2005), Low particulate organic carbon export in the frontal zone of the Southern Ocean (Indian sector) revealed by 234Th, *Deep-Sea Res. I*, *52*(1), 51–68.

Dall'Olmo, G., J. Dingle, L. Polimene, R. J. Brewin, and H. Claustre (2016), Substantial energy input to the mesopelagic ecosystem from the seasonal mixed-layer pump, *Nat. Geosci.*, *9*(11), 820–823.

DeVries, T., and F. W. Primeau (2011), Dynamically and observationally constrained estimates of water-mass distributions and ages in the global ocean, *J. Phys. Oceanogr.*, *41*(12), 2381–2401.

Dunne, J. P., R. A. Armstrong, A. Gnanadesikan, and J. L. Sarmiento (2005), Empirical and mechanistic models for the particle export ratio, *Global Biogeochem. Cycles*, *19*(4).

Emerson, S. (2014), Annual net community production and the biological carbon flux in the ocean, *Global Biogeochem. Cycles*, *28*(1), 14–28.

Eppley, R. W., and B. J. Peterson (1979), Particulate organic matter flux and planktonic new production in the deep ocean, *Nature*, *282*(5740), 677.

Fu, W., and F. Primeau (2017), Application of a fast Newton–Krylov solver for equilibrium simulations of phosphorus and oxygen, *Ocean Model.*, *119*, 35–44.

Galbraith, E. D., and A. C. Martiny (2015), A simple nutrient-dependence mechanism for predicting the stoichiometry of marine ecosystems, *Proc. Natl. Acad. Sci. USA*, *112*(27), 8199–8204.

Garcia, H., R. Locarnini, T. Boyer, J. Antonov, O. Baranova, M. Zweng, J. Reagan, and D. Johnson (2014), World Ocean Atlas 2013, Volume 4: Dissolved Inorganic Nutrients (Phosphate, Nitrate, Silicate), NOAA Atlas NESDIS, vol. 76, edited by S. Levitus, 25 pp, *US Gov. Print. Off., Washington, DC*.

Gardner, W. D., S. P. Chung, M. J. Richardson, and I. D. Walsh (1995), The oceanic mixed-layer pump, *Deep-Sea Res. II*, *42*(2-3), 757–775.

Giering, S. L., R. Sanders, R. S. Lampitt, T. R. Anderson, C. Tamburini, M. Boutrif, M. V. Zubkov, C. M. Marsay, S. A. Henson, K. Saw, et al. (2014), Reconciliation of the carbon budget in the oceans twilight zone, *Nature*, *507*(7493), 480.

Guidi, L., L. Legendre, G. Reygondeau, J. Uitz, L. Stemmann, and S. A. Henson (2015), A new look at ocean carbon remineralization for estimating deepwater sequestration, *Global Biogeochem. Cycles*, *29*(7), 1044–1059.

Hansell, D. A., C. A. Carlson, D. J. Repeta, and R. Schlitzer (2009), Dissolved organic matter in the ocean: A controversy stimulates new insights, *Oceanography*, *22*(4), 202–211.

Hansell, D. A., C. A. Carlson, and R. Schlitzer (2012), Net removal of major marine dissolved organic carbon fractions in the subsurface ocean, *Global Biogeochem. Cycles*, *26*(1).

Harrison, C. S., M. C. Long, N. S. Lovenduski, and J. K. Moore (2018), Mesoscale effects on carbon export: A global perspective, *Global Biogeochem. Cycles*, *32*(4), 680–703.

Henson, S. A., R. Sanders, E. Madsen, P. J. Morris, F. Le Moigne, and G. D. Quartly (2011), A reduced estimate of the strength of the ocean's biological carbon pump, *Geophys. Res. Lett.*, *38*(4).

Henson, S. A., R. Sanders, and E. Madsen (2012), Global patterns in efficiency of particulate organic carbon export and transfer to the deep ocean, *Global Biogeochem. Cycles*, *26*(1).

KawaKami, H., M. C. Honda, K. Matsumoto, T. Fujiki, and S. Watanabe (2010), East-west Distribution of POC fluxes estimated from ^{234}Th in the northern North Pacific in Autumn, *J. oceanogr.*, *66*, 71–83.

Kriest, I., and A. Oschlies (2008), On the treatment of particulate organic matter sinking in large-scale models of marine biogeochemical cycles, *Biogeosciences (BG)*, *5*, 55–72.

Kwon, E. Y., F. Primeau, and J. L. Sarmiento (2009), The impact of remineralization depth on the air–sea carbon balance, *Nat. Geosci.*, *2*(9), 630.

Lalande, C., S. B. Moran, P. Wassmann, J. M. Grebmeier, and L. W. Cooper (2008), 234Th-derived particulate organic carbon fluxes in the northern Barents Sea with comparison to drifting sediment trap fluxes, *J. Marine Syst.*, *73*(1-2), 103–113.

Lam, P. J., and J. K. Bishop (2007), High biomass, low export regimes in the southern ocean, *Deep-Sea Res. II*, *54*(5-7), 601–638.

Laurenceau-Cornec, E. C., T. W. Trull, D. M. Davies, S. G. Bray, J. Doran, F. Planchon, F. Carlotti, M.-P. Jouandet, A.-J. Cavagna, A. M. Waite, and S. Blain (2015), The relative importance of phytoplankton aggregates and zooplankton fecal pellets to carbon export: insights from free-drifting sediment trap deployments in naturally iron-fertilised waters near the Kerguelen Plateau, *Biogeosciences*, *12*(4), 1007–1027.

Laws, E. A., and K. Maiti (2019), The relationship between primary production and export production in the ocean: Effects of time lags and temporal variability, *Deep-Sea Res. I*, *148*, 100–107.

Laws, E. A., P. G. Falkowski, W. O. Smith, H. Ducklow, and J. J. McCarthy (2000), Temperature effects on export production in the open ocean, *Global Biogeochem. Cycles*, *14*(4), 1231–1246.

Laws, E. A., E. D'Sa, and P. Naik (2011), Simple equations to estimate ratios of new or export production to total production from satellite-derived estimates of sea surface temperature and primary production, *Limnol. Oceanogr. Methods*, *9*(12), 593–601.

Le Moigne, F., A. J. Poulton, S. A. Henson, C. J. Daniels, G. M. Fragoso, E. Mitchell, S. Richier, B. C. Russell, H. E. Smith, G. A. Tarling, et al. (2015), Carbon export efficiency and phytoplankton community composition in the Atlantic sector of the Arctic Ocean, *J. Geophys. Res. Oceans*, *120*(6), 3896–3912.

Le Moigne, F. A., C. M. Moore, R. J. Sanders, M. Villa-Alfageme, S. Steigenberger, and E. P. Achterberg (2014), Sequestration efficiency in the iron-limited North Atlantic: Implications for iron supply mode to fertilized blooms, *Geophys. Res. Lett.*, *41*(13), 4619–4627.

Le Moigne, F. A., S. A. Henson, E. Cavan, C. Georges, K. Pabortsava, E. P. Achterberg, E. Ceballos-Romero, M. Zubkov, and R. J. Sanders (2016), What causes the inverse relationship between primary production and export efficiency in the Southern Ocean?, *Geophys. Res. Lett.*, *43*(9), 4457–4466.

Le Moigne, F. A. C., S. A. Henson, R. J. Sanders, and E. Madsen (2013), Global database of surface ocean particulate organic carbon export fluxes diagnosed from the ^{234}Th

technique, *Earth Syst. Sci. Data*, *5*(2), 295–304.

Letscher, R., J. Moore, Y. Teng, and F. Primeau (2015), Variable C: N: P stoichiometry of dissolved organic matter cycling in the Community Earth System Model, *Biogeosciences*, *12*(1), 209.

Letscher, R. T., and J. K. Moore (2015), Preferential remineralization of dissolved organic phosphorus and non-redfield dom dynamics in the global ocean: Impacts on marine productivity, nitrogen fixation, and carbon export, *Global Biogeochem. Cycles*, *29*(3), 325–340.

Maiti, K., M. A. Charette, K. O. Buesseler, and M. Kahru (2013), An inverse relationship between production and export efficiency in the Southern Ocean, *Geophys. Res. Lett.*, *40*(8), 1557–1561.

Martin, J. H., G. A. Knauer, D. M. Karl, and W. W. Broenkow (1987), VERTEX: carbon cycling in the Northeast Pacific, *Deep-Sea Res. I*, *34*(2), 267–285.

Mawji, E., R. Schlitzer, E. M. Dodas, C. Abadie, W. Abouchami, R. F. Anderson, O. Baars, K. Bakker, M. Baskaran, N. R. Bates, et al. (2015), The geotraces intermediate data product 2014.

Moriarty, R., E. Buitenhuis, C. L. Quéré, and M.-P. Gosselin (2013), Distribution of known macrozooplankton abundance and biomass in the global ocean, *Earth Syst. Sci. Data*, *5*(2), 241–257.

Mouw, C. B., A. Barnett, G. A. McKinley, L. Gloege, and D. Pilcher (2016), Global ocean particulate organic carbon flux merged with satellite parameters, *Earth Syst. Sci. Data*, *8*(2), 531.

Owens, S. A., K. O. Buesseler, and K. W. W. Sims (2011), Re-evaluating the ^{238}U-salinity relationship in seawater: Implications for the ^{238}U^{234}Th disequilibrium method, *Mar. Chem.*, *127*(1-4), 31–39.

Owens, S. A., S. Pike, and K. O. Buesseler (2015), Thorium-234 as a tracer of particle dynamics and upper ocean export in the Atlantic Ocean, *Deep-Sea Res. II*, *116*, 42–59.

Planchon, F., A.-J. Cavagna, D. Cardinal, L. A. , and F. Dehairs (2013), Late summer particulate organic carbon export and twilight zone remineralisation in the Atlantic sector of the Southern Ocean, *Biogeosciences*, *10*, 803–820.

Planchon, F., D. Ballas, A. Cavagna, A. Bowie, D. Davies, T. Trull, E. Laurenceau-Cornec, P. Van Der Merwe, and F. Dehairs (2015), Carbon export in the naturally iron-fertilized Kerguelen area of the Southern Ocean based on the ^{234}Th approach, *Biogeosciences*, *12*(12), 3831–3848.

Primeau, F. W., M. Holzer, and T. DeVries (2013), Southern Ocean nutrient trapping and the efficiency of the biological pump, *J. Geophys. Res. Ocean.*, *118*(5), 2547–2564.

Roca-Martí, M., V. Puigcorbé, M. H. Iversen, M. R. van der Loeff, C. Klaas, W. Cheah, A. Bracher, and P. Masqué (2017), High particulate organic carbon export during the decline of a vast diatom bloom in the Atlantic sector of the Southern Ocean, *Deep-Sea Res. II*, *138*, 102–115.

Rosengard, S. Z., P. J. Lam, W. M. Balch, M. E. Auro, S. Pike, D. Drapeau, and B. Bowler (2015), Carbon export and transfer to depth across the Southern Ocean Great Calcite Belt, *Biogeosciences*, *12*(13), 3953–3971.

Roshan, S., and T. DeVries (2017), Efficient dissolved organic carbon production and export in the oligotrophic ocean, *Nat. Commun.*, *8*(1), 2036.

Rutgers van der Loeff, M., J. Friedrich, and U. V. Bathmann (1997), Carbon export during the Spring Bloom at the Antarctic Polar Front, determined with the natural tracer ^{234}Th, *Deep-Sea Res. II*, *44*(1-2), 457–478.

Rutgers van der Loeff, M., P. H. Cai, I. Stimac, A. Bracher, R. Middag, M. B. Klunder, and S. M. A. C. van Heuven (2011), ^{234}Th in surface waters: Distribution of particle export flux across the Antarctic Circumpolar Current and in the Weddell Sea during the GEOTRACES expedition ZERO and DRAKE, *Deep-Sea Res. II*, *58*(25-26), 2749–2766.

Santschi, P., L. Guo, I. Walsh, M. Quigley, and M. Baskaran (1999), Boundary exchange and scavenging of radionuclides in continental margin waters of the Middle Atlantic Bight: implications for organic carbon fluxes, *Cont. Shelf Res.*, *19*, 609–636.

Savoye, N., C. Benitez-Nelson, A. B. Burd, J. K. Cochran, M. Charette, K. O. Buesseler, G. A. Jackson, M. Roy-Barman, S. Schmidt, and M. Elskens (2006), ^{234}Th sorption and export models in the water column: A review, *Mar. Chem.*, *100*(3-4), 234–249.

Schlitzer, R., R. F. Anderson, E. M. Dodas, M. Lohan, W. Geibert, A. Tagliabue, A. Bowie, C. Jeandel, M. T. Maldonado, W. M. Landing, et al. (2018), The GEOTRACES Intermediate Data Product 2017, *Chem. Geol.*, *493*, 210–223.

Siegel, D. A., K. O. Buesseler, S. C. Doney, S. F. Sailley, M. J. Behrenfeld, and P. W. Boyd (2014), Global assessment of ocean carbon export by combining satellite observations and food-web models, *Global Biogeochem. Cycles*, *28*(3), 181–196.

Teng, Y. C., F. W. Primeau, J. K. Moore, M. W. Lomas, and A. C. Martiny (2014), Global-scale variations of the ratios of carbon to phosphorus in exported marine organic matter, *Nat. Geosci.*, *7*(12), 895–898.

Thomalla, S., R. Turnewitsch, M. Lucas, and A. Poulton (2006), Particulate organic carbon export from the North and South Atlantic gyres: The ^{234}Th/^{238}U disequilibrium approach, *Deep-Sea Res. II*, *53*(14-16), 1629–1648.

Wang, W.-L., J. K. Moore, A. C. Martiny, and F. W. Primeau (2019a), Convergent estimates of marine nitrogen fixation, *Nature*, *566*(7743), 205.

Wang, W.-L., C. Lee, and F. W. Primeau (2019b), A Bayesian statistical approach to inferring particle dynamics from in-situ pump POC and chloropigment data from the Mediterranean Sea, *Mar. Chem.*, *214*, 103,654.

Westberry, T., M. Behrenfeld, D. Siegel, and E. Boss (2008), Carbon-based primary productivity modeling with vertically resolved photoacclimation, *Global Biogeochem. Cycles.*, *22*(2), GB2024.

Zhou, K., S. D. Nodder, M. Dai, and J. Hall (2012), Insignificant enhancement of export flux in the highly productive subtropical front, east of New Zealand: a high resolution study of particle export fluxes based on ^{234}Th: ^{238}U disequilibria, *Biogeosciences*, *9*(3), 973–992.

Zweng, M., J. Reagan, J. Antonov, R. Locarnini, A. Mishonov, T. Boyer, H. Garcia, O. Baranova, D. Johnson, D.Seidov, and M. Biddle (2013), World Ocean Atlas 2013, Volume 2: Salinity, NOAA Atlas NESDIS 74, edited by S. Levitus, 39 pp.

Table 1. Comparison of C:P export ratios to reference values. $(C:P)_P$ is carbon to phosphorus ratio of sinking particles and $(C:P)_D$ is the ratio of dissolved organic matter.

‡ bulk C:P (DOC + POC) ratio from *Teng et al.* [2014].

† This study.

⋆ dissolved C:P ratio form *Letscher and Moore* [2015].

N.A.: not available.

Regions	$(C:P)^{\ddagger}_{bulk}$	$(C:P)^{\dagger}_{P}$	$(C:P)^{\dagger}_{D}$	$(C:P)^{\star}_{D}$
N. Atlantic gyre	355^{+65}_{-59}	159^{181}_{136}	448^{526}_{355}	380±188
Equatorial Atlantic	81^{+21}_{-18}	105^{121}_{89}	191^{243}_{167}	186±29
S. Atlantic gyre	163^{+49}_{-42}	138^{160}_{117}	212^{292}_{150}	130±18
Southern Ocean	91^{+11}_{-9}	105^{121}_{89}	102^{127}_{81}	N.A.
S. Indian gyre	115^{+42}_{-35}	153^{175}_{129}	140^{201}_{106}	N.A.
Equatorial Indian Ocean	103^{+30}_{-26}	112^{130}_{112}	195^{301}_{146}	N.A.
S. Pacific gyre	138^{+37}_{-33}	139^{161}_{118}	171^{255}_{104}	140±121
Equatorial Pacific	83^{+15}_{-13}	104^{120}_{88}	176^{240}_{143}	N.A.
N. Pacific gyre	176^{+33}_{-30}	137^{159}_{116}	283^{356}_{207}	247±15
N. Subpolar Pacific	86^{+23}_{-20}	92^{107}_{78}	127^{172}_{95}	120±33
N. subpolar Atlantic	63^{+24}_{-20}	87^{100}_{74}	97^{127}_{71}	347±33

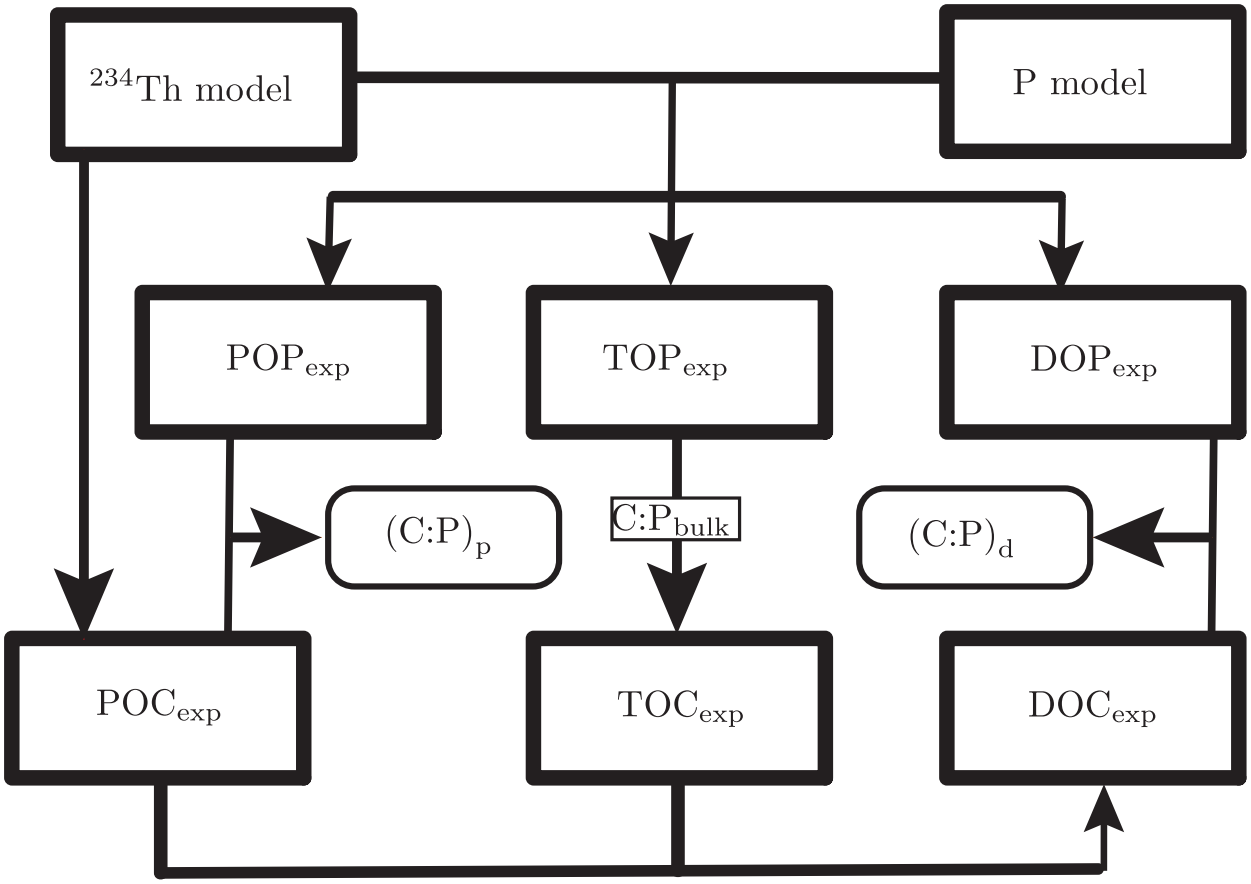

Figure 1. Schematic representation of the joint ^{234}Th and phosphorus model. The model parameters are jointly constrained using observed DIP and ^{234}Th concentration/activity. The black arrows show the flow of information for the calculation of each export component. C:P$_{bulk}$ is bulk C:P export ratio, which is the average of C:P ratios of *Teng et al.* [2014] and *Wang et al.* [2019a].

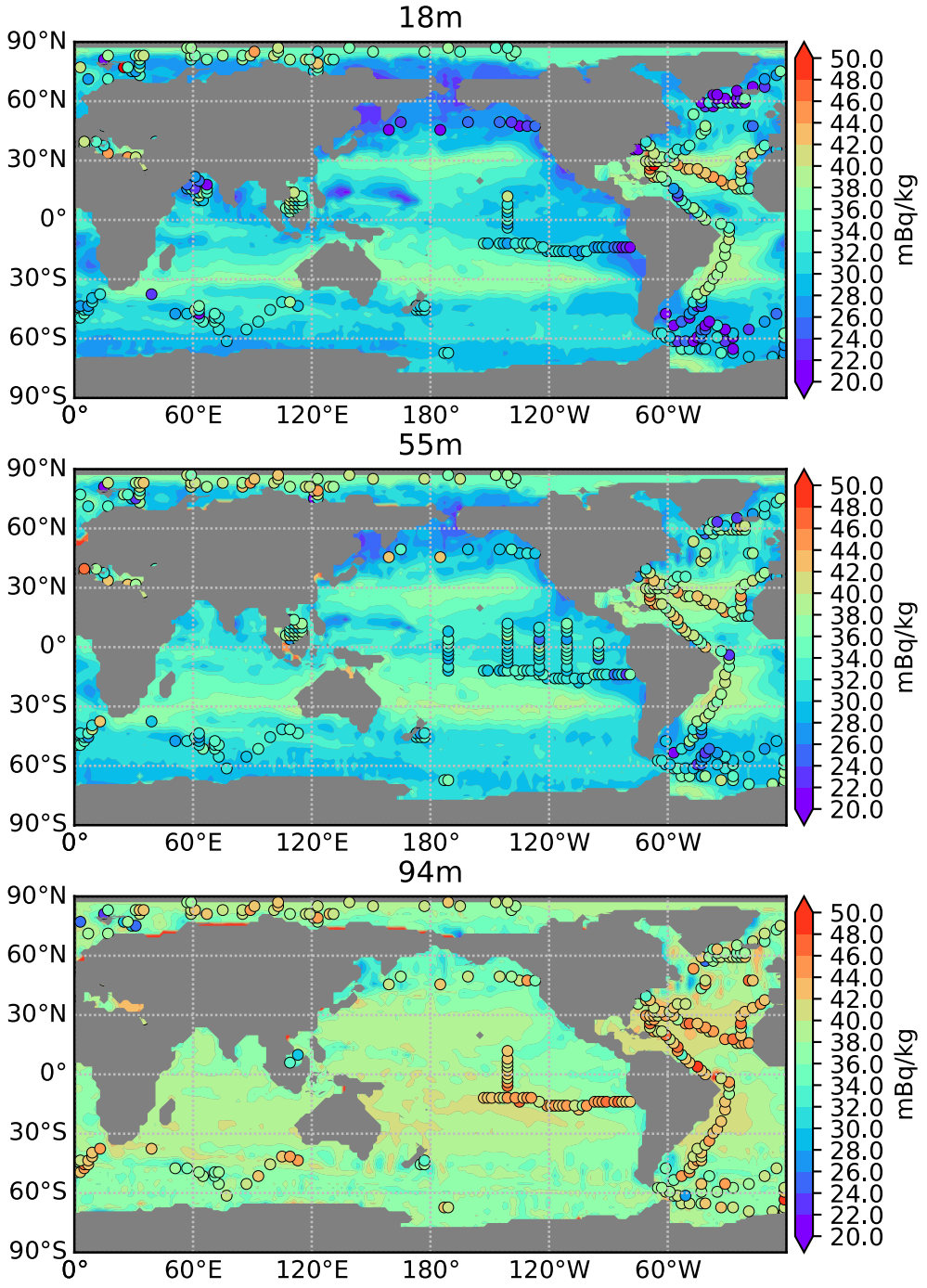

Figure 2. Distribution of total ^{234}Th activity. Total ^{234}Th activity at top three model layers overlaid with in situ observation using the same color scale. See Appendix A for data source.

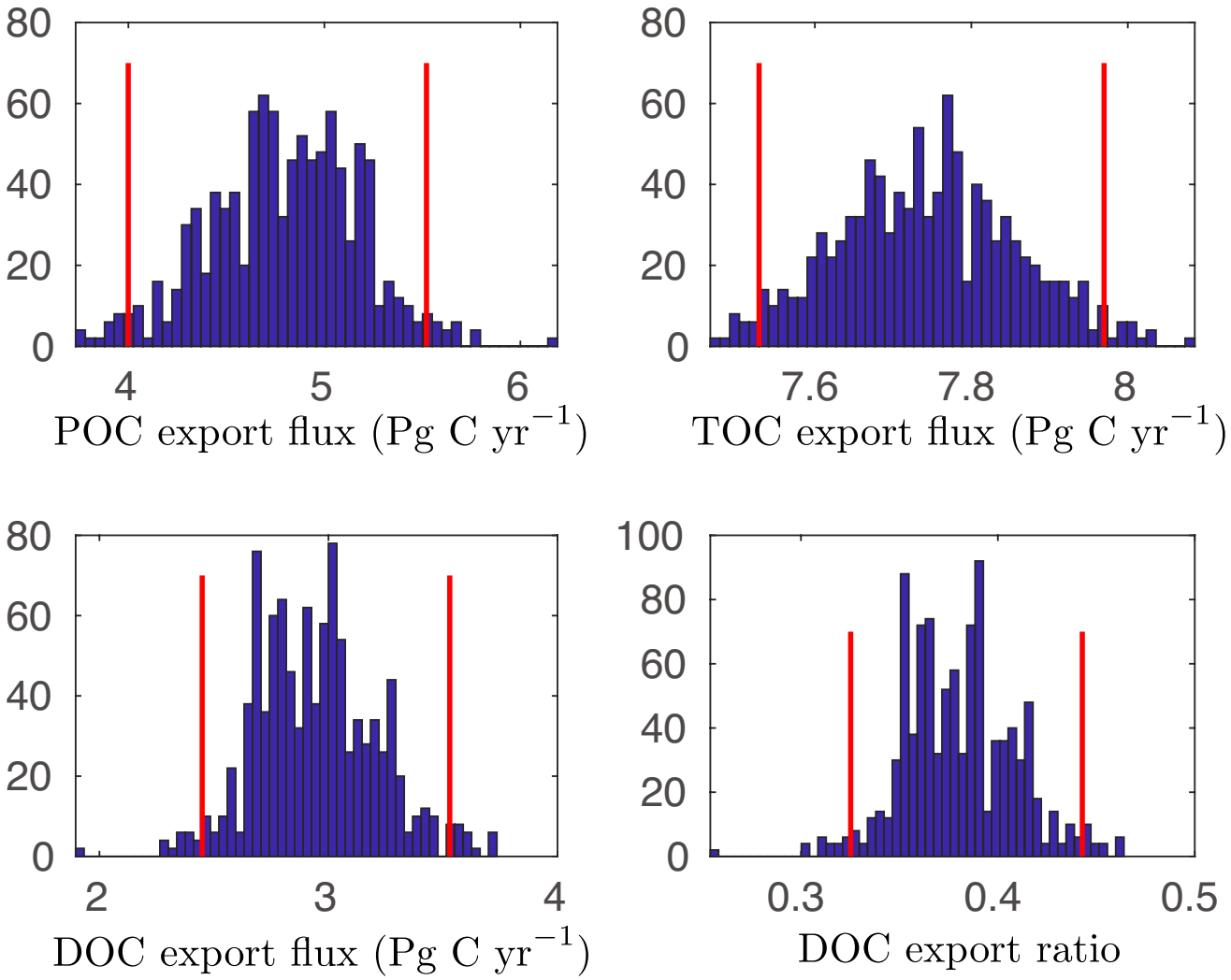

Figure 3. Histogram shows total POC, TOC, and DOC distributions based on Monte Carlo simulation. In the test, we randomly select parameter combinations ($\theta_i \sim N(\hat{\theta}, \Sigma)$), with which we recalculated POC, TOC, and DOC export flux. A sample size of 1000 model runs is shown in the histogram.

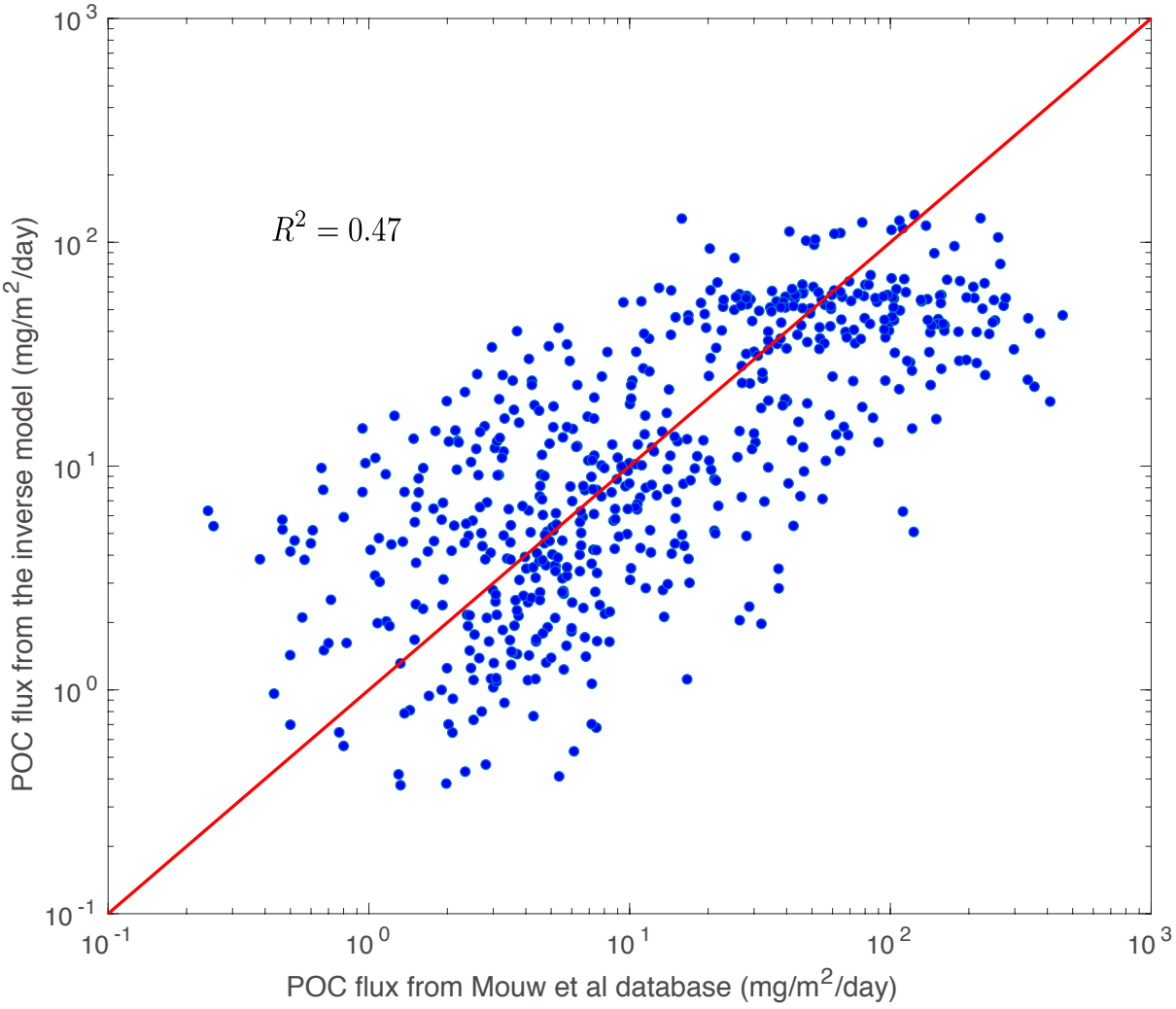

Figure 4. Comparison of model inferred POC flux with *Mouw et al.* [2016], of which 96% were measured using sediment trap, and the other 4% using 234Th method. $R^2 = 0.47$ on log scale. The red line is 1:1 line.

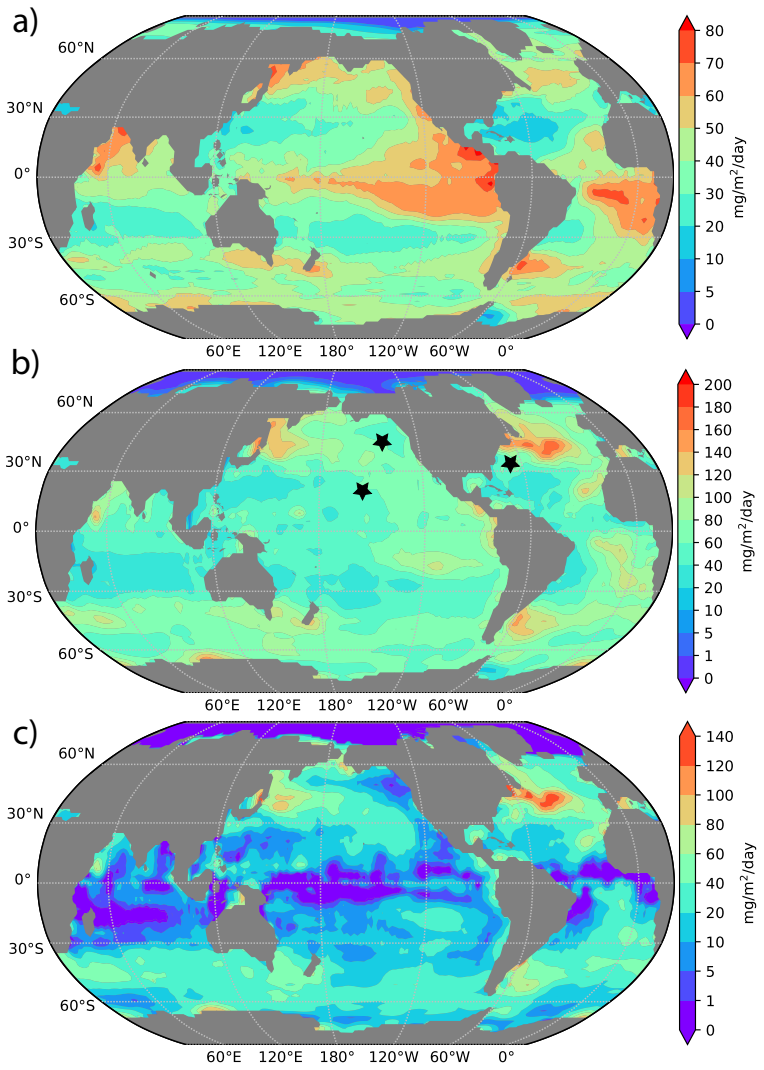

Figure 5. Contour plots of model inferred POC (a) flux at 100 m, TOC (b) and DOC (c) export fluxes at 114 m. POC flux is constrained using model ^{234}Th distribution. Note that the original POC flux is calculated at 114 m because this is the depth of the third grid box. We then scaled POC flux to 100 m using Martin curve function and optimal b values. TOC flux is calculated based on the phosphorus model and spatially varying C:P ratio from *Teng et al.* [2014] and *Wang et al.* [2019a]. The three black dots indicate locations of three time-series sites, Ocean Station Papa (OSP), Hawaii Ocean Time-series (HOT), and Bermuda Atlantic Time-series Study (BATS). DOC export flux is the difference between TOC and POC export fluxes.

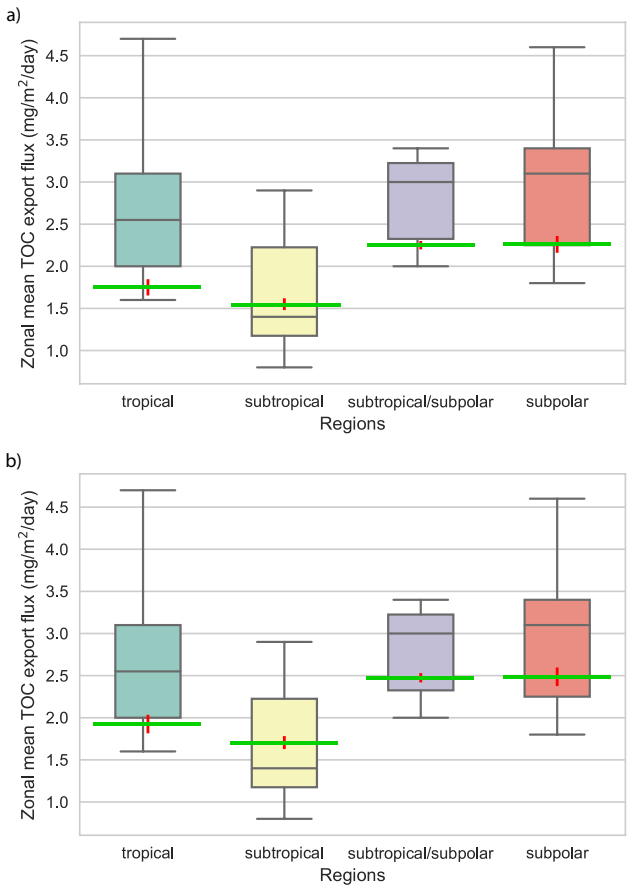

Figure 6. Comparisons of TOC export flux to Annual Net Community Production (ANCP, mol C m^{-2} yr^{-1}). ANCP over an annual cycle equals to the flux of biogenic organic matter, TOC export flux in our model. Global ocean is divided into four regions, tropical (0-15°), subtropical (15-30°), subtropical/subpolar (30-45°), and subpolar (45-60°) according to *Emerson* [2014]. The zonally averaged data denoted by the box plots are from Table 1 of *Emerson* [2014]. Boxplots display the 25(Q1), 50(Q2), and 75(Q3) percentiles, the whiskers show the "minimum" and "maximum", which are defined as Q1-1.5IQR and Q3+1.5IQR where IQR is the range from 25(Q1) to 75(Q3) percentile. Flux of figure (a) is at 114 m, and flux of figure (b) is scaled up to 100 m by applying a 10% factor. The blank circles with red errorbars (median with 95% CI) are zonally average value from our model.

Appendix A: Data

Total ^{234}Th (particulate+dissolved) activity are obtained by compiling data from GEOTRACES [*Mawji et al.*, 2015; *Schlitzer et al.*, 2018] and from published reference (Table A1). Globally, we have a total of 3723 measurements from the literature and 2262 from US GEOTRACES. After binning these observations into the grid of the Ocean Circulation Inverse Model (OCIM) (2°× 2° resolution with 24 vertical levels), there are 2521 grid boxes with ^{234}Th measurements. ^{234}Th based upper ocean (<150 m) POC flux data are from https://www.pangaea.de/ [*Le Moigne et al.*, 2013], with new data from *Black et al.* [2018]. The inverse model also uses salinity, phosphate, and net primary production (NPP) data. The salinity and inorganic phosphorus data are from World Ocean Atlas 2013 [*Zweng et al.*, 2013; *Garcia et al.*, 2014]. Net primary production (NPP) data used to parameterize biological phosphate uptake are satellite-derived carbon based primary production data (MODIS CbPM) [*Westberry et al.*, 2008]. Sediment POC flux data are downloaded from https://doi.pangaea.de/10.1594/PANGAEA.855600 [*Mouw et al.*, 2016], and are binned into the grid of OCIM.

Appendix B: Sensitivity tests

In the model, we use particulate organic phosphorus [POP] as a proxy for sinking particles that carries ^{234}Th out of the surface ocean. We acknowledge that phosphorus is a small portion of sinking particles, other components, such as particulate organic carbon, opal, and calcium carbonate, also absorb dissolved thorium. Here we run multiple sensitivity tests to demonstrate that our model is robust to $R_{M:P}$, sinking mass to phosphorus ratio.

In the first test, we converted POP to POC by applying spatially variable C:P ratios based on *Galbraith and Martiny* [2015]. We tested if the converted [POC] is a better proxy for the sinking

particles because carbon is a larger portion of sinking particles compared to phosphorus. However, we reject this model based on its poor fit to the observation (Fig. A4). One possible reason for the poor performance is that POC may not represent sinking mass better than phosphorus. One can imagine that in high productivity regions, such as the Southern Ocean, the C:P ratio is low [e.g. *Galbraith and Martiny*, 2015], but total sinking mass (sum of organic matter, calcium carbonate and opal etc.) to P ratio can be high because of high diatom activities.

In a second experiment, we formulated two equations for the sinking mass to phosphorus ratio ($R_{M:P}$), in which sinking mass is proportional to the ambient phosphorus concentration. Two parameters controlling the "slope" (S) and "intercept" (R_{min}) are optimized in the inversion.

$$\begin{aligned} R_{M:P} &= R_{min} + S(1 - \tanh([\mathrm{DIP}])), \\ R_{M:P} &= R_{min} - S[\mathrm{DIP}]. \end{aligned} \tag{B1}$$

We found that the optimal value of R_{min} correlates with the adsorption and desorption rate constants, and the optimal value of S is less than 1×10^{-2}. Thus, we obtain virtually the same POC and DOC export patterns as in the control model. Based on the current data constraints, we did not find evidence indicating that $R_{M:P}$ has significantly spatial variations. The implied gradients are sufficiently weak to be ignored.

Table A1. Sampling time, area, number of samples (N), methods of measurement (Methods), and reference of ^{234}Th data. Sampling time and locations of GEOTRACES samples can be retrieved from the following website: https://www.egeotraces.org.

Year	Regions	*N*	Methods	Reference
Oct.-Nov.(1992)	Southern Ocean	124	Part.+Diss.	*Rutgers van der Loeff et al.* [1997]
Feb. May, Aug. (1996) Feb. (1997)	Subarctic Pacific	161	Part.+Diss.	*Charette et al.* [1999]
May (1993) Jun-Jul.(1994)	Middle Atlantic Bight	64	Part.+Diss.	*Santschi et al.* [1999]
Jan.-Feb.(1999)	Southern Ocean	50	Part.+Diss.	*Coppola et al.* [2005]
Jan.-Feb.(2002)	Southern Ocean	120	Total	*Buesseler et al.* [2005]
Apr.-May (2004)	Atlantic (50S-50N)	88	Total	*Thomalla et al.* [2006]
Jul.(2003),May(2005)	Arctic	38	Total	*Lalande et al.* [2008]
Apr.-May (2004)	South China Sea	174	Total	*Cai et al.* [2008]
Jun.-Aug.(2004),Jul.-Aug.(2005)	North Atlantic	678	Total	*Buesseler et al.* [2008]
Sep.-Oct.(2005)	North Pacific	31	Total	*KawaKami et al.* [2010]
Jul.-Oct.(2007)	Arctic	236	Total	*Cai et al.* [2010]
Feb.-Mar.(2008)	Southern Ocean	197	Total	*Rutgers van der Loeff et al.* [2011]
May-Jun. (2008)	South-west Pacific	147	Total	*Zhou et al.* [2012]
Jan.-Mar.(2008)	Bonus-GoodHope section	175	Total	*Planchon et al.* [2013]
Oct.-Nov.(2011)	Southern Ocean	185	Total	*Planchon et al.* [2015]
Austral Summer (2011,2012)	Southern Ocean	318	Total	*Rosengard et al.* [2015]
Jan.-Feb.(2012)	Southern Ocean	107	Part.+Diss.	*Roca-Martí et al.* [2017]
2009	North Atlantic	97	Total	*Le Moigne et al.* [2013]
Jul.-Aug.(2010)	North Atlantic	195	Total	*Le Moigne et al.* [2014]
Jun.-Jul.(2012)	Arctic	98	Total	*Le Moigne et al.* [2015]
Jan.-Feb.(2013)	Southern Ocean	127	Total	*Le Moigne et al.* [2016]

Table A2. Most probable parameter values. κ_d is DOP remineralization rate constant. α and β are the two parameters in the function that scales NPP to DIP assimilation rate (Eq. 2). κ_1 and κ_{-1} are thorium adsorption and desorption rate constant. The optimal b values are displayed in Fig.A1.

Parameters	values	units
κ_d	$(3.78^{+0.06}_{-0.05})\times10^{-8}$	s^{-1}
α	$2.50^{+0.20}_{-0.20}$	s^{-1}
β	$0.71^{+0.01}_{-0.01}$	unitless
κ_1	$(2.69^{+0.04}_{-0.04})\times10^{-5}$	m^3 $mmol^{-1}s^{-1}$
κ_{-1}	$(9.19^{+0.24}_{-0.24})\times10^{-7}$	s^{-1}

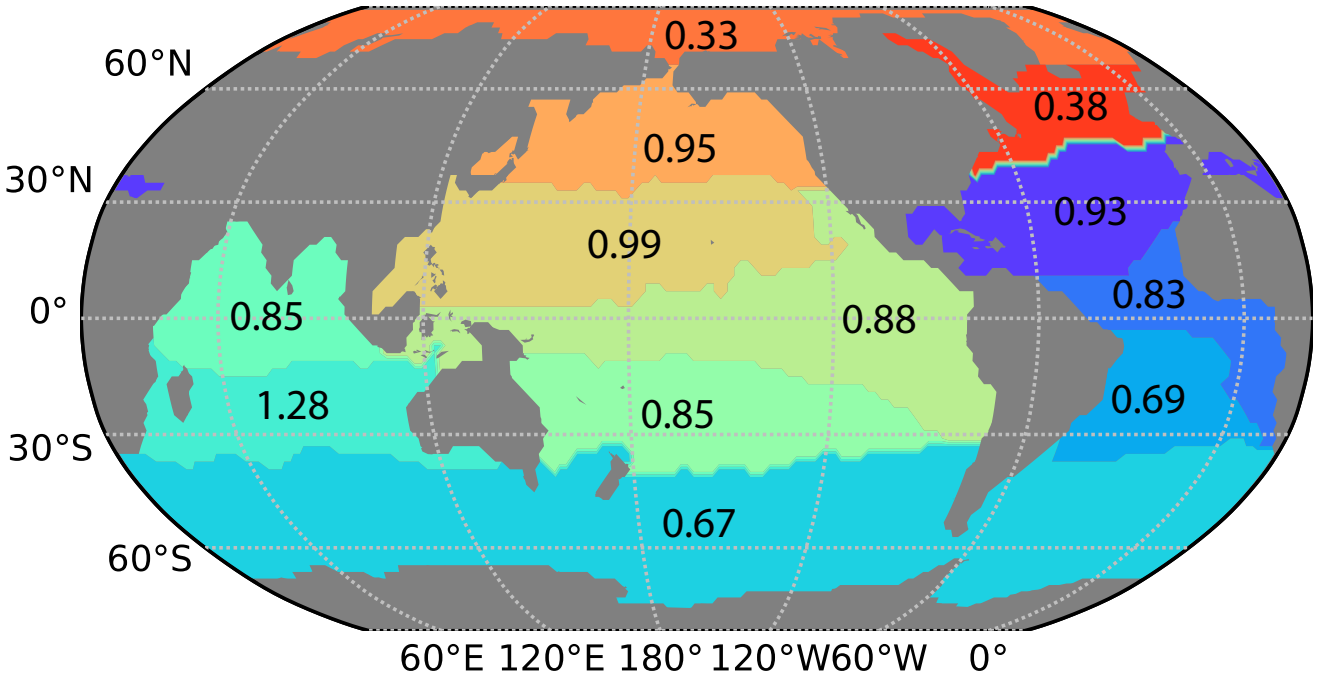

Figure A1. Optimal b values for each region based on *Teng et al.* [2014] division.

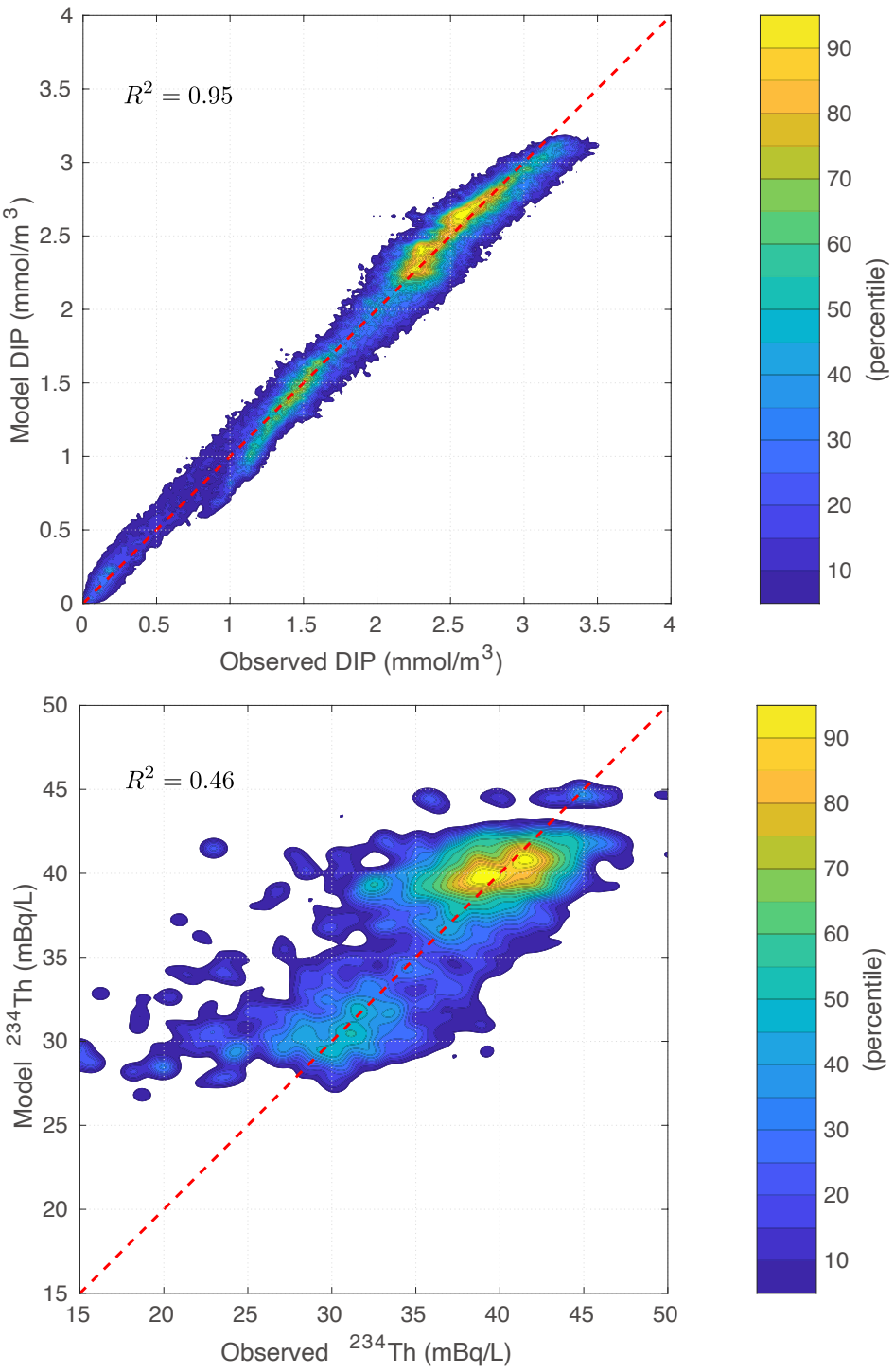

Figure A2. Comparison of model tracers with observed ones. 1) Model DIP versus WOA2013 climatology DIP concentration. 2) Model total ^{234}Th (dissolved + particulate) versus observation.

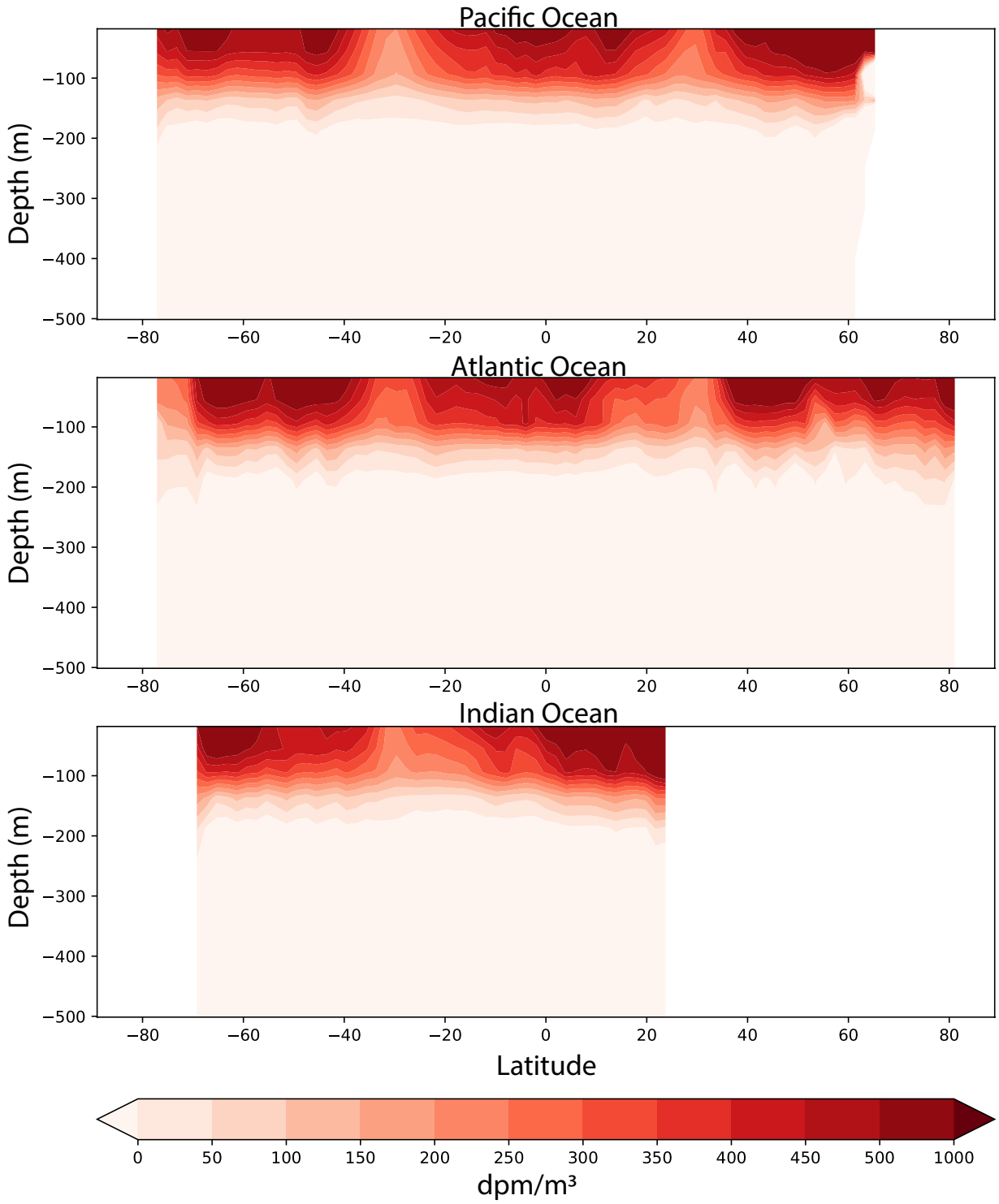

Figure A3. Zonal mean difference between ^{238}U and ^{234}Th for the three major basins.

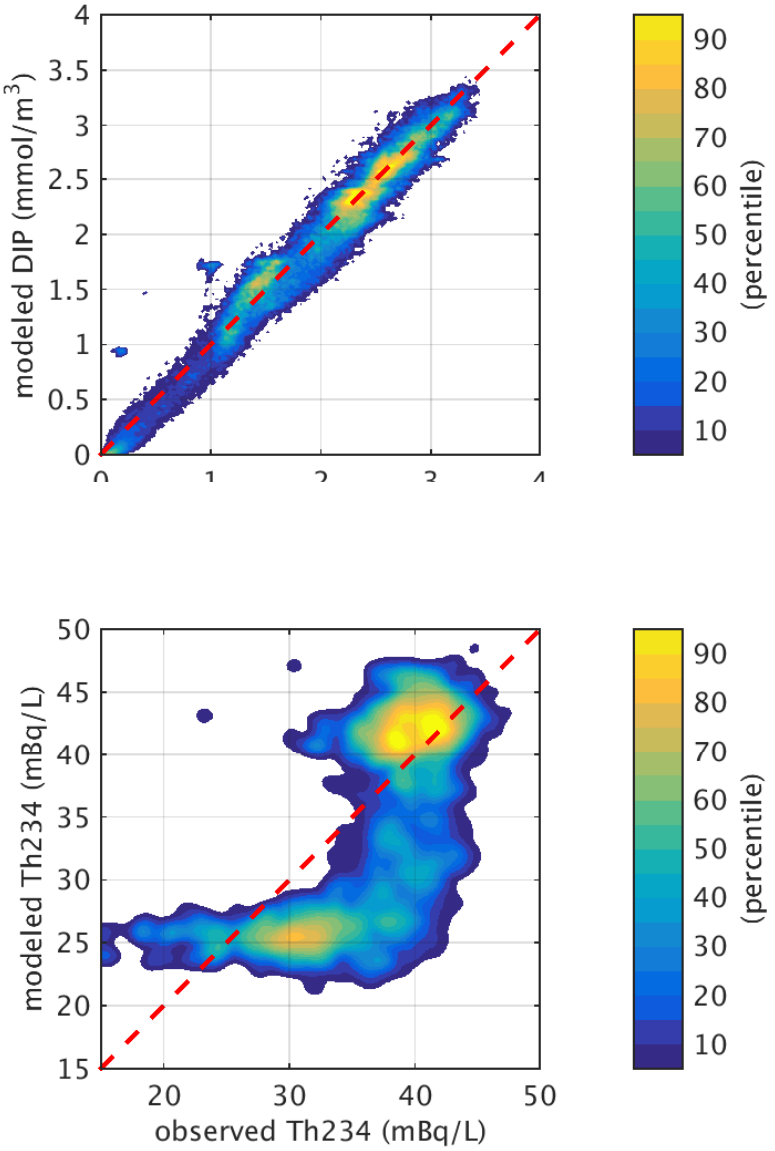

Figure A4. Comparison of observed and modeled tracers based on Galbraith and Martiny *Galbraith and Martiny* [2015] C:P parameterization. 1) Model DIP versus WOA2013 climatology DIP concentration. 2) Model total ^{234}Th (dissolved + particulate) versus observation.